Full Text View

Volume 32, Issue 1 (January 2002)

Journal of Physical Oceanography
Article: pp. 240–264 | Abstract | PDF (393K)

Ocean Turbulence. Part II: Vertical Diffusivities of Momentum, Heat, Salt, Mass, and Passive Scalars

V. M. Canuto

NASA Goddard Institute for Space Studies and Department of Applied Physics, Columbia University, New York, New York

A. Howard, Y. Cheng, and M. S. Dubovikov

NASA Goddard Institute for Space Studies, New York, New York

(Manuscript received July 31, 2000, in final form June 21, 2001)

DOI: 10.1175/1520-0485(2002)032<0240:OTPIVD>2.0.CO;2

ABSTRACT

A Reynolds stress–based model is used to derive algebraic expressions for the vertical diffusivities $K_\alpha(\alpha = m, h, s)$ for momentum, heat, and salt. The diffusivities are expressed as

$$K_\alpha(R_\rho, N, \mathrm{Ri}^{\mathrm{T}}, \epsilon)$$

in terms of the density ratio $R_\rho = \alpha_s \partial S/\partial z(\alpha_T \partial T/\partial z)^{-1}$, the Brunt–Väisälä frequency $N^2 = -g\rho^{-1}{}_0 \partial\rho/\partial z$, the Richardson number $\mathrm{Ri}^{\mathrm{T}} = N^2/\Sigma^2$ (Σ is the shear), and the dissipation rate of kinetic energy ϵ. The model is valid both in the mixed layer (ML) and below it. Here R_ρ and N are computed everywhere using the large-scale fields from an ocean general circulation model while Ri^{T} is contributed by resolved and unresolved shear. In the ML, the wind-generated large-scale shear dominates and can be computed within an OGCM. Below the ML, the wind is no longer felt and small-scale shear dominates. In this region, the model provides a new relation $\mathrm{Ri}^{\mathrm{T}} = cf(R_\rho)$ with $c \approx 1$ in lieu of Munk's suggestion $\mathrm{Ri}^{\mathrm{T}} \approx c$. Thus, below the ML, the K_α become functions of R_ρ, N, and ϵ.

The dissipation ϵ representing the physical processes responsible for the mixing, which are different in different parts of the ocean, must also be expressed in terms of the large-scale fields. In the ML, the main source of

stirring is the wind but below the ML there is more than one possible source of stirring. For regions away from topography, one can compute ϵ using a model for internal waves. On the other hand, near topography, one must employ different expressions for ϵ. In agreement with the data, the resulting diffusivities are location dependent rather than universal values.

Using North Atlantic Tracer Release Experiment (NATRE) data, the authors test the new diffusivities with and without an OGCM. The measured diffusivities are well reproduced. Also, a set of global T and S profiles is computed using this model and the KPP model. The profiles are compared with Levitus data. In the North Atlantic, at 24°N, the meridional overturning is close to the measured values of 17 ± 4 Sv and 16 ± 5 Sv (Sv $\equiv 10^6$ m^3 s^{-1}). The polar heat transport for the North Atlantic Ocean, the Indo–Pacific Ocean, and the global ocean are generally lowered by double diffusion. The freshwater budget is computed and compared with available data.

1. Introduction: Physical motivation

In Canuto et al. (2001b, hereafter Part I) we employed the Reynolds stress formalism to construct a model for the heat and momentum diffusivities. The goal of this paper is to extend the same formalism to include double diffusive processes, that is, the possibility that heat and salt diffusivity may differ. Although we are not the first to study this problem (Gargett and Holloway 1992; Zhang et al. 1999; Zhang and Schmitt 2000), there are two motivations for a new treatment. First, the NATRE data (North Atlantic Tracer Release Experiment: Ledwell et al. 1993, 1998) have provided the first set of measured salt, heat, and tracer diffusivities at different ocean depths. The second motivation is of methodological nature: recent advances in turbulence modeling allow a unified treatment of momentum, heat, and salt with the same formalism. Thus, the use in an OGCM of a diffusivity model that has been tested on the NATRE data may help answer the question of Ledwell et al. (1998): how are the heat and salt diffusivities K_h and K_s modulated by the density ratio R_ρ and what effect does this modulation have on the general circulation?

Using the Reynolds stress formalism, we derive algebraic expressions for the diffusivities $K_{m,h,s}$ (momentum, heat, salt) as functions of N (Brunt–Väisälä frequency), R_ρ (density ratio), Ri^T (Richardson number), and ϵ (dissipation rate of kinetic energy):

$$K_\alpha(R_\rho, N, \mathrm{Ri}^T, \epsilon), \qquad \alpha = m, h, s. \quad (1a)$$

Relations (1a) are valid both in the mixed layer (ML) and below it. While the functions R_ρ and N are computable everywhere using the large-scale temperature and salinity fields from an OGCM, Ri^T is contributed by both large-scale (resolved) and small-scale (unresolved) shear. In the ML (mixed layer), the strongest shear is the wind-generated large-scale shear, which is computable within an OGCM. Below the ML, where the wind effects are no longer felt, it is the small-scale shear generated by internal waves that dominates. In that regime, the present model provides a new relation $\mathrm{Ri}^T = cf(R_\rho)$ with $c \approx 1$ in lieu of Munk's suggestion that $\mathrm{Ri}^T \approx c$. Thus, below the ML, Eq. (1a) reduces to

$$K_\alpha(R_\rho, N, \epsilon), \qquad \alpha = m, h, s. \quad (1b)$$

The dissipation ϵ, which is not computed by an OGCM, plays a physically important role. Since mixing requires a source of energy, there is a necessity to exhibit the energy required to sustain the mixing processes. This point has been discussed by Munk and Wunsch (1998), Wunsch (2000), and Egbert and Ray (2000).

The available sources of energy are different at different depths and in different parts of the ocean and so are the resulting diffusivities. In the ML, the primary energy source is the wind shear, while below the ML there are several energy sources. Figure 3 of Ledwell et al. (2000) shows deep ocean diffusivities at various locations. For example, at the NATRE site (away from boundaries) the diffusivities are around ~ 0.1 cm^2 s^{-1} while values 40 times larger were measured in the Brazilian Basin (Polzin et al. 1997). Internal wave breaking processes are thought to be the primary source of mixing in the open ocean, and models exist that provide the corresponding ϵ (e.g., the Gregg–Henyey–Polzin model). However, the ϵ representing tidal dissipation over topography (Bell 1975; Armi and Millard 1976; Müller and Xu 1992; Jayne and St. Laurent 2001) or geothermal heating on global ocean circulation (Adcroft et al. 2001) requires appropriate models describing those processes.

Over the years, relations (1b) were represented with different models. Gargett and Holloway (1992) used a constant K_s/K_h ratio. Large et al. (1994) used $K_s/K_h = 1.43$ but Merryfield et al. (1999) pointed out that the correct relation is $K_s/K_h = 1.43R_\rho^{-1}$. Zhang et al. (1988, hereafter ZHS) used phenomenological expressions for $K_{h,s}(R_\rho)$ (Schmitt 1981; Kunze 1987, 1990; Fedorov 1988; Kelley 1984, 1990), but St. Laurent and Schmitt (1999, Fig. 16) showed that two such models (Kunze 1987, 1990) predict an R_ρ dependence not in accord with NATRE data; the ad hoc model by Schmitt (1981) has the correct R_ρ dependence but is too diffusive. All authors find that double diffusion lowers the meridional transport.

The structure of the paper is as follows. In sections 2 to 8 we derive the expressions for the diffusivities K_α and discuss the physics of the model and the role of the dissipation timescales, the weak and strong mixing regimes, the existence of a critical R_ρ(cr) above which one has strong salt fingers, and the inclusion of the internal wave field. In section 10, we compare ours with previous models and in section 11 we discuss general features of the diffusivities. In sections 12 and 13 we compare the model results with NATRE data with and without an OGCM. In section 14 we exhibit the T–S profiles for the global ocean (and for different ocean basins), the meridional streamfunction, the polar heat transport, and the freshwater budgets. In sections 15 and 16 we present a discussion and future improvements of the model.

2. Diffusivities: General features

Global ocean models solve the dynamic equations for the large-scale velocity U_i, temperature T, and salinity S (in Cartesian coordinates, i and j take the values 1, 2, 3):

$$\frac{\partial}{\partial t}U_i + \frac{\partial}{\partial x_j}(U_iU_j + \overline{u_i'' u_j''}) = \cdots \qquad (2a)$$

$$\frac{\partial T}{\partial t} + \frac{\partial}{\partial x_i}(U_iT + \overline{u_i''T''}) = \cdots \qquad (2b)$$

$$\frac{\partial S}{\partial t} + \frac{\partial}{\partial x_i}(U_iS + \overline{u_i''s''}) = \cdots. \qquad (2c)$$

Since the velocity, temperature, and salinity fields have also fluctuating components u_i'', T'', s'', nonlinear interactions give rise to the second order moments $\overline{u_i''u_j''}$ (momentum fluxes or Reynolds stresses), $\overline{u_i''T''}$ (heat fluxes), and $\overline{u_i''s''}$ (salinity fluxes). The overbar means averaging performed over the grid cell and the time step of the OGCM. A local turbulence model (in section 16 we discuss nonlocal models) provides the vertical fluxes:

$$\overline{w''u''} = -K_m\frac{\partial U}{\partial z}, \qquad \overline{w''T''} = -K_h\frac{\partial T}{\partial z},$$

$$\overline{w''s''} = -K_s\frac{\partial S}{\partial z}, \qquad (2d)$$

where $K_\alpha(\alpha = m, h, s)$ are the diffusivities given as a function of

$$K_\alpha = K_\alpha(R_\rho, N, \mathrm{Ri}^T, \epsilon), \qquad (2e)$$

where R_ρ is the density ratio and Ri^T is the total Richardson number:

$$R_\rho = \alpha_s\frac{\partial S}{\partial z}\left(\alpha_T\frac{\partial T}{\partial z}\right)^{-1}, \qquad \mathrm{Ri}^T = \frac{N^2}{\Sigma_T^2}. \qquad (3a)$$

The $\alpha_{T,S}$ are the thermal expansion and haline contraction coefficients and

$$N^2 = -\frac{g}{\rho_0}\frac{\partial \rho}{\partial z} = g\alpha_T \frac{\partial T}{\partial z}(1 - R_\rho) = N_h^2(1 - R_\rho). \quad (3b)$$

The total shear $\Sigma_T = (\Sigma^2 + \Sigma'^2)^{1/2}$ is contributed by resolved large scales (that dominate in the ML) and by small unresolved scales that dominate below the ML. We have

$$\Sigma^2 = 2(\Sigma_{ij}\Sigma_{ij}), \qquad \Sigma_{ij} = \frac{1}{2}\left(\frac{\partial U_i}{\partial x_j} + \frac{\partial U_j}{\partial x_i}\right). \quad (3c)$$

The diffusivities K_ρ, K_c that enter the mass flux $\overline{w''\rho''}$ and the concentration flux $\overline{w''c''}$:

$$\overline{w''\rho''} = -K_\rho \frac{\partial \rho}{\partial z}, \qquad \overline{w''c''} = -K_c \frac{\partial C}{\partial z} \quad (3d)$$

are given by

$$K_\rho = (K_h - K_s R_\rho)(1 - R_\rho)^{-1} \quad (3e)$$

$$K_c = (K_s + K_h R_\rho)(1 + R_\rho)^{-1}. \quad (3f)$$

Equation (3e) follows from using $\rho''/\rho = -\alpha_T T'' + \alpha_s s''$ in the first of (3d) and using both (2d) and (3b). Equation (3f) requires some discussion. The competing effects of the T–S fields on the density ρ are reflected in the minus sign in the numerator of (3e). Here T–S are active scalars since they couple to ρ, which couples to the velocity, and thus ultimately T–S affect turbulence. On the other hand, a passive scalar does not affect either the density or the velocity field. For example, the SF_6 used at the NATRE site did not affect materially the density or the velocity field by which it was passively transported. Equation (3f) assumes that a concentration field behaves like "spiciness," which, by definition, is density neutral.

As shown below, the Reynolds-stress-based model provides the following expressions:

$$K_\alpha = 2E^2\epsilon^{-1}S_\alpha, \quad (4a)$$

where E is turbulent kinetic energy, ϵ its rate of dissipation, and the dimensionless functions S_α are called "structure functions" (Part I; Burchard and Bolding 2001; Burchard and Deleersnijder 2001). In studies of mixing below the ML, an alternative representation is the one due to Osborn and Cox (1972) and Osborn (1980):

$$K_\alpha = \Gamma_\alpha \epsilon N^{-2}, \qquad \Gamma_\alpha \equiv \frac{1}{2}(\tau N)^2 S_\alpha, \quad (4b)$$

where $\tau = 2E/\epsilon$ is the dynamical timescale and Γ_α are mixing efficiencies. This representation is particularly convenient for it highlights ϵ, which is different in different parts of the ocean. For either representation, a model is needed to provide the functions E, ϵ, S_α, and Γ_α. Finally, the mixing model to be discussed below is valid for the following cases: SF (salt fingers: $\partial S/\partial z > 0$, $\partial T/\partial z > 0$, $R_\rho > 0$, $\mathrm{Ri}^T > 0$, $0 < R_\rho < 1$); DC (diffusive convection: $\partial S/\partial z < 0$, $\partial T/\partial z < 0$, $R_\rho > 0$, $\mathrm{Ri}^T > 0$, $1 < R_\rho$); DS (doubly stable: $\partial S/\partial z < 0$, $\partial T/\partial z > 0$, $R_\rho < 0$, $\mathrm{Ri}^T > 0$); DU (doubly unstable: $\partial S/\partial z > 0$, $\partial T/\partial z < 0$, $R_\rho < 0$, $\mathrm{Ri}^T < 0$). We recall that due to the definitions of Ri^T and N^2 in Eqs. (3a,b), $\mathrm{Ri}^T > 0$ corresponds to dynamical stability while $\mathrm{Ri}^T < 0$ corresponds to dynamical instability.

3. The Reynolds stress model

Historically, the Reynolds stress model (RSM) has been widely used to treat turbulence problems since the early 1940s [for a series of review articles, see Gatski et al. (1993)]. In addition to engineering studies, RSM have been widely applied to atmospheric and ocean studies, primarily in the ML (Part I). In this paper, we consider mixing due to three gradients $\partial U/\partial z$,

$\partial T/\partial z$, and $\partial S/\partial z$. In Part I, we treated the case of velocity and temperature while Zeman and Lumley (1982, 1983) treated the case of temperature and salinity. Even with three gradients, the final expressions of the diffusivities are still algebraic. The overall procedure can be summarized as follows. Consider the Navier–Stokes equations for the velocity field and the equations for T, S. The fields are written as the sum of a resolved (large scale) plus an unresolved (small scale) fluctuating part. Substituting and averaging leads to the equations for the resolved fields, Eqs. (2a)–(2c). To obtain the dynamic equations for the fluctuating u''_i, T'', s'' one subtracts Eqs. (2a)–(2c) from the original equations for the full fields. Multiplying the equation for T'' (s'') by u''_i and that for u''_i by T'' (s''), and the equations for T'' and s'' by the same T'', s'', averaging and summing the results, one obtains the dynamic equation for the required second-order moments $\overline{u''_i u''_j}$, $\overline{u''_i T''}$, $\overline{u''_i s''}$, $\overline{T''^2}$, $\overline{s''^2}$, and $\overline{T''s''}$. Using the notation, $U_{i,j} \equiv \partial U_i/\partial x_j$ and $D/Dt \equiv \partial/\partial t + U_i \partial/\partial x_i$, the dynamic equations are

Traceless Reynolds stresses: $b_{ij} = \overline{u''_i u''_j} - 2/3E\delta_{ij} \equiv \tau_{ij} - (2/3)E\delta_{ij}$:

$$\frac{D}{Dt}b_{ij} = -\frac{8}{15}E\Sigma_{ij} - (1 - p_1)\Omega_{ij} + (1 - p_2)Z_{ij} + \frac{1}{2}g(\alpha_T L_{ij} - \alpha_s M_{ij}) - 5\tau^{-1}b_{ij}. \quad (5)$$

The tensors L_{ij}, M_{ij} represent buoyancy, Ω_{ij} represents shear Σ_{ij}, and Z_{ij} represents vorticity $2V_{ij} \equiv U_{i,j} - U_{j,i}$. They are defined as follows:

$$L_{ij} \equiv \lambda_i J^h_j + \lambda_i J^h_j - \frac{2}{3}\delta_{ij}\lambda_k J^h_k,$$

$$M_{ij} \equiv \lambda_i J^S_j + \lambda_j J^S_i - \frac{2}{3}\delta_{ij}\lambda_k J^S_k$$

$$\Omega_{ij} \equiv b_{ik}\Sigma_{jk} + b_{jk}\Sigma_{ik} - \frac{2}{3}\delta_{ij}\Sigma_{km}b_{km}$$

$$Z_{ij} \equiv b_{ik}V_{jk} + b_{jk}V_{ik}, \quad (6)$$

where $\lambda_i = -(g\rho)^{-1}\partial\overline{p}/\partial x_i$, $\overline{p}$ being the mean pressure. Heat flux, $J^h_i = \overline{u''_i T''}$:

$$\frac{D}{Dt}J^h_i = -\tau_{ij}\frac{\partial T}{\partial x_j} - J^h_j U_{i,j} - (2\alpha_T\Psi - \alpha_s\overline{s''T''})\frac{\partial\overline{p}}{\partial x_i} - \tau^{-1}_{p\theta}J^h_i \quad (7)$$

Temperature variance, $\Psi = \overline{T''^2}$:

$$\frac{D\Psi}{Dt} = -J^h_i\frac{\partial T}{\partial x_i} - 2\tau^{-1}_\theta\Psi \quad (8)$$

Salinity variance, $\Phi = \overline{s''^2}$:

$$- \tau_{ps}^{-1} J_i^s \qquad (9)$$

Salinity flux, $J^S_i = \overline{u''_i s''}$:

$$\frac{D}{Dt} J_i^s = -\tau_{ij} \frac{\partial S}{\partial x_j} - J_j^s U_{i,j} - (\alpha_T \overline{T''s''} - 2\alpha_s \Phi) \frac{\partial \overline{p}}{\partial x_i}$$

$$- \tau_{ps}^{-1} J_i^s \qquad (10)$$

Temperature–salinity correlation, $\overline{T''s''}$:

$$\frac{D}{Dt} \overline{T''s''} = -\left(J_i^s \frac{\partial T}{\partial x_i} + J_i^h \frac{\partial S}{\partial x_i} \right) - \tau_{s\theta}^{-1} \overline{T''s''}. \qquad (11)$$

In the absence of salt, Eqs. (5)–(11) coincide with those of Part I. In the absence of shear, they coincide with Eqs. (1) of Zeman and Lumley (1982, 1983). Before presenting the solution of Eqs. (5)–(11), it is useful to discuss their physical interpretation. We begin with Eqs. (8), (9), and (11). The time variation is governed by the combination of a source term (the first term in the right-hand side of each equation) and dissipation by molecular forces (the last term). In a thermally unstably stratified flow, the z gradient of T in (8) is negative while the z component of the heat flux is positive and the first term is positive, acting as a source. An analogous argument applies to the salt variance Φ. In the case of the heat flux, the first term in (7), which acts as a source, is given by the interaction of the Reynolds stresses with the T gradient, the second term represents the interaction of the heat flux with shear while the third term represents the positive contribution of potential energy $\sim \overline{T}''^2$. Analogous interpretations apply to the other equations. The last terms in Eqs. (5)–(11) represent the overall dissipation effects. When written in units of the dynamic timescale τ, they are denoted by

$$\pi_{1,2,3,4,5} = (\tau_{ps}, \tau_{s\theta}, \tau_s, \tau_{p\theta}, \tau_\theta)\tau^{-1}, \qquad \tau = 2E\epsilon^{-1}. \quad (12)$$

The physical role of the π can be better understood after we have solved Eqs. (5)–(11).

4. Solution of Eqs. (5)–(11)

We shall consider the case in which the only nonzero gradients are in the z direction, $\partial/\partial x_i \longrightarrow \delta_{i3} \partial/\partial z$. Even so, the time-dependent Eqs. (5)–(11) are very difficult to solve or to use in an OGCM. For that reason, we consider a quasistationary state that we approximate with $\partial/\partial t = 0$. Equations (5)–(11) then become a system of linear, coupled, algebraic equations, which we solved using the MAPLE V (University of Waterloo, 1981–1990; Symbolic Math Toolboxes available online at www.mathworks.com). When $\overline{w''u''}$, $\overline{w''T''}$, and $\overline{w''s''}$ are cast in the form (2d) and each of the K_α is written as in (4a), the structure functions S_α turn out to be momentum:

$$DS_m = \frac{8}{75}(12 + a_1 n^2 + a_2 nc + a_3 c^2 + a_4 n + a_5 c), \qquad (13a)$$

heat:

$$DS_h = \frac{4}{15}\pi_4(1 + b_1 c + b_2 n)$$

$$\times (60 + b_3 y + b_4 c + b_5 n), \qquad (13b)$$

salt:

$$\times (60 + b_3 y + b_4 c + b_5 n). \qquad (13c)$$

The dimensionless denominator D is given by

$$D = 24 + d_1 y n^2 + d_2 y n c + d_3 y c^2 + d_4 n^3 + d_5 n^2 c + d_6 n c^2 + d_7 c^3 + d_8 y n + d_9 y c + d_{10} n^2 + d_{11} n c + d_{12} c^2 + d_{13} y + d_{14} n + d_{15} c. \qquad (14)$$

The dimensionless functions representing stratification, salt gradient, and shear are

$$x \equiv (\tau N)^2 (1 - R_\rho)^{-1}, \qquad n = -\pi_2 \pi_3 x,$$

$$c = \pi_3^2 R_\rho x,$$

$$y = \frac{4}{25} x (1 - R_\rho)(\mathrm{Ri}^T)^{-1}. \qquad (15)$$

The variables a_k b_k and d_k depend on the π and are given in appendices A and B.

a. Eddy turnover time, τ

The eddy turnover time τ entering Eqs.(15) is obtained by solving the equation for the turbulent kinetic energy $E = \tau_{ii}$:

$$\frac{DE}{Dt} = P_s + P_b - \epsilon, \qquad (16a)$$

where the shear and buoyancy production terms are defined as

$$P_s = -\tau_{ij} U_{i,j},$$

$$P_b = -g \overline{\rho}^{-1} \overline{\rho'' w''} = g \alpha_T J^h - g \alpha_s J^s, \qquad (16b)$$

where we have used the relation $\rho''/\rho = -\alpha_T T'' + \alpha_S s\&PrimeI;$. In the stationary limit, Eq. (16a) becomes production equals dissipation. Using (2d), (3a,b), and (4a), we obtain

$$2(\tau N)^{-2} \mathrm{Ri}^T = S_m - \mathrm{Ri}^T (1 - R_\rho)^{-1} (S_h - S_s R_\rho). \quad (16c)$$

Using the $S_{m,h,s}$, Eq. (16c) yields $(\tau N)^2$, x, n, c, y, S_α, and Γ_α as functions of Ri^T and R_ρ.

b. Heat to salt diffusivity ratio K_h/K_s

The ratio of heat to salt diffusivities has a particularly simple form. Using Eq. (3) of appendix A and Eqs. (13b,c), a short algebra gives

$$\frac{K_h}{K_s} = \frac{\pi_4}{\pi_1} \frac{1 - \pi_1 \pi_3 x R_\rho + \pi_1 \pi_2 x (1 + R_\rho)}{1 + \pi_4 \pi_5 x - \pi_2 \pi_4 x (1 + R_\rho)}. \qquad (17a)$$

Since $x \sim (\tau N)^2$, a large x means that $\tau > N^{-1}$: the shortest timescale is due to the strong stratification, which makes turbulence weak. On the other hand, a small x means weak stratification and stronger turbulence. Thus, we have the asymptotic regimes weak turbulence:

$$\frac{K_h}{K_s} = \frac{(\pi_2 - \pi_3)R_\rho + \pi_2}{\pi_5 - \pi_2 - \pi_2 R_\rho} \qquad (17b)$$

strong turbulence:

$$\frac{K_h}{K_s} = \frac{\pi_4}{\pi_1} = \frac{\tau_{p\theta}}{\tau_{ps}}. \qquad (17c)$$

The first conclusion from (17b,c) is that the timescales π that contribute to the weak and strong cases are different. Purely dissipative timescales τ_s, $\tau_\theta(\pi_{3,5})$ are expected to affect only the weak case when molecular forces are maximal and Eq. (17b) confirms the expectation. On the other hand, in the strong limit, we have only $\tau_{p\theta}$ and τ_{ps}, which are contributed by both molecular and pressure correlations (subscript p). The latter come about as follows. In deriving the dynamic equations for the heat and salt fluxes $\overline{w''T'}$ and $\overline{w''s''}$, one employs the Navier–Stokes equations for w'', which entails the pressure gradient $\partial p''/\partial z$. Using Poisson's equation, pressure terms can be written in terms of the velocity field so as to assure that the latter is nondivergent, $\partial u_i''/\partial x_i = 0$. Thus, pressure correlations, when viewed as part of the nonlinear interactions, are an important component of the strong limit, as confirmed by Eq. (17c).

5. Critical R_ρ

In the ocean, salt fingers coexist with shear, which in the deep ocean and away from boundaries is due to internal wave breaking. It is therefore important to define the regimes where shear and salt fingers dominate. As for the latter, Schmitt and Evans (1978) have shown that only "modes with $R_\rho \geq R_\rho(\text{cr}) = 1/2$ become strongly established" and Zhang et al. (1998) state that a "reasonable value based on observations" is $R_\rho(\text{cr}) = 0.64$ and thus salt fingers are found in the regime:

$$0.64 \leq R_\rho \leq 1. \qquad (18a)$$

Below $R_\rho(\text{cr})$, mixing is sustained primarily by shear. To determine $R_\rho(\text{cr})$, we consider the zero shear limit of Eq. (16c), $2x^{-1} = S_s R_\rho - S_h$. Using the $S_{s,h}$ from (13b,c), a series of algebraic steps yields the simple equation:

$$A + Bx^{-1} - x^{-2} = 0 \qquad (18b)$$

$$\frac{15}{7}A = \pi_1(\mu - \pi_2\pi_4)R_\rho - \pi_4(\eta + \pi_1\pi_2 R_\rho) - \frac{15}{7}(\eta\mu + \pi_1\pi_2^2\pi_4 R_\rho)$$

$$\frac{15}{7}B = \pi_1 R_\rho - \pi_4 - \frac{15}{7}(\eta + \mu),$$

$$\eta \equiv \pi_1(\pi_2 - \pi_3 R_\rho),$$

$$\mu \equiv \pi_4(\pi_5 - \pi_2 R_\rho). \qquad (18c)$$

Since $R_\rho(\text{cr})$ corresponds to zero turbulent kinetic energy, $E \rightarrow 0$ or $x \rightarrow \infty$, Eq. (18b) becomes $A = 0$ which in turn gives

$$\xi = \left(1 + \frac{15}{7}\pi_5\right)\left(1 + \frac{15}{7}\pi_3\right)^{-1}. \qquad (18d)$$

6. The dissipative timescales π

a. General expressions

It is known that the RSM is unable to determine the dissipative timescales π. This is because the RSM does not provide the spectra of the different turbulence variables but only their integral over all wavenumbers while the determination of the dissipation timescales requires the spectra. In most geophysical applications (Mellor and Yamada 1982), the π were considered adjustable parameters and data were used to quantify them. In the presence of salt, there are three additional timescales τ_{ps}, $\tau_{s\theta}$, and τ_s and the data may not be sufficient to determine all the π's. In addition, even if one could fix a set of π's, there is no guarantee that they would apply in circumstances different from those used for their determination. We shall therefore attempt to evaluate the π's. Since $(k^2\kappa_T)^{-1}$ is the thermal timescale of an eddy of size k^{-1}, one has in general (Monin and Yaglom 1971, 1975):

$$\tau_\theta^{-1} = 2\kappa_T\left(\int k^2 E_T(k)\, dk\right)(\overline{T''}^2)^{-1},$$

$$\frac{1}{2}\overline{T''}^2 \equiv \int E_T(k)\, dk, \qquad (19a)$$

where $E_T(k)$ is the spectrum of the temperature variance. Analogous expressions hold true for salt with the changes $\kappa_T \rightarrow \kappa_s$, $E_T(k) \rightarrow E_s(k)$, $T'' \rightarrow s''$. As for the definition of $\tau_{p\theta}$, it is arrived at after integrating the two-point closure dynamic equations for the spectrum $J(k)$ so that $J_h = \int J(k)\, dk$. A rather long derivation (Canuto and Dubovikov 1996a,b; 1997, hereafter CD) leads to the following results (ν is the molecular viscosity):

$$\tau_{p\theta}^{-1} = \left[\int k^2(\nu_d + \chi_d)J(k)\, dk\right]J_h^{-1} \qquad (19b)$$

$$\nu_d(k) = \left(\nu^2 + \frac{2}{5}\int_k^\infty p^{-2}E(p)\, dp\right)^{1/2} \qquad (19c)$$

$$b\chi_d - \nu_d = (b\kappa_T - \nu)\left(\frac{a\kappa_T + \nu}{a\chi_d + \nu_d}\right)^{a/b}. \qquad (19d)$$

Here $\nu_d(k)$ and $\chi_d(k)$ are the dynamical or eddy, viscosity, and conductivity, which depend on the wavenumber k. Relations (19b–d) are valid for any ν and κ_T. Since the derivation of relations (19b–d) and of the coefficients $a = 0.42$ and $b = 0.72$ is rather involved (CD96–97) and cannot be repeated here, we shall try to give a physical interpretation. We begin with (19a) and the corresponding one for salt. The molecular diffusivity κ_T is independent of the size of the eddy $\sim k^{-1}$ and is therefore outside the integral. On the other hand, as already discussed after Eq. (17c), $\tau_{p\theta}$ is contributed by both molecular and pressure correlations. The latter become part of the nonlinear interactions whose closure brings about an "enhanced" eddy viscosity ν_d and conductivity χ_d. Since the latter are the sum of a turbulent part (from the nonlinear interactions) plus a molecular part, they are called dynamical (thus the subscript d). Contrary to their molecular counterparts, dynamical diffusivities depend on the eddy size k^{-1}, and therefore are inside the integral.

As for Eq. (19c), the smaller the eddy (the larger the k), the smaller is the integral and the more $\nu_d(k) \rightarrow \nu$, as indeed

expected for small eddies. Equation (19c) entails the turbulent kinetic energy spectrum given by Kolmogorov law $E(k) = \mathrm{Ko}\,\epsilon^{2/3}k^{-5/3}$, where $1.5 \leq \mathrm{Ko} \leq 1.8$. A physical interpretation of (19c) is as follows. Consider the Reynolds number $\mathrm{Re} = UL\nu^{-1}$. Using $U \sim E^{1/2}$ and the size of the largest eddy $L \sim k_0^{-1}$, we also have $\mathrm{Re} \sim E^{1/2}k_0^{-1}\nu^{-1}$ and $\mathrm{Re}^2 \sim Ek_0^{-2}\nu^{-2}$. Consider now a spectral Reynolds number squared $\mathrm{Re}^2_*(k)$ defined as

$$\mathrm{Re}^2_*(k) = E(k)k^{-2}\nu^{-2},$$

$$\mathrm{Re}^2(k) \equiv \int_k^\infty \mathrm{Re}^2_*(p)\,dp. \qquad (19e)$$

This allows us to rewrite (19c) in a more transparent form (we neglect numerical factors)

$$\nu_d(k) = \nu[1 + \mathrm{Re}^2(k)]^{1/2}. \quad (19f)$$

When Re is small, the eddy viscosity reduces to the molecular ν; when the flow is very turbulent and $\mathrm{Re} > 1$, ν_d is considerably larger than ν. Next, consider Eq. (19d) that yields the dynamical (eddy) conductivity $\chi_d(k)$ once the dynamical viscosity is known from (19c). Equation (19d) encompasses two limiting cases that previously had been treated separately. When molecular effects are negligible, Eq. (19d) gives $\chi_d = b^{-1}\nu_d$. In the opposite case, Eq. (19c) yields $\nu_d \longrightarrow \nu$ and substitution in (19d) shows that $\chi_d = \kappa_T$. Finally, we remark that the k integrations in Eqs. (19b,c) extend up to the dissipation wave scale $\lambda_d = (\nu^3\epsilon^{-1})^{1/4}$ and that the ratio L/λ_d depends on Re because of the (model independent) relation $L/\lambda_d = \mathrm{Re}^{3/4}$. The larger Re, the larger the ratio L/λ_d and the wider is the interval over which one must integrate the spectra. As the above relations indicate, to proceed one needs to know the various spectra, a topic that we discuss next.

b. Weak turbulence

In a low Re regime $L/\lambda_d \sim O(1)$, and the spectra are so narrow as to be almost delta functions, $E(k) = E\delta(k - k_0)$, which is Prandtl's mixing length model where one large eddy prevails. Equations (19) and the ones for salinity, then yield (Zeman and Lumley 1982, 1983):

$$\pi_1 \equiv \tau_{ps}/\tau = (1 + \kappa_s\nu^{-1})^{-1},$$

$$\pi_2 \equiv \tau_{s\theta}/\tau = \nu(\kappa_s + \kappa_T)^{-1},$$

$$\pi_3 \equiv \tau_s/\tau = \nu\kappa_s^{-1},$$

$$\pi_4 \equiv \tau_{p\theta}/\tau = (1 + \kappa_T\nu^{-1})^{-1},$$

$$\pi_5 \equiv \tau_\theta/\tau = \nu/\kappa_T. \qquad (20a)$$

The appearance of ν is due to the fact that $\tau = 2E/\epsilon$ where by definition $\epsilon = 2\nu\int k^2E(k)\,dk$. Use of (20a) in (17b) gives

$$\frac{K_h}{K_s} \sim \frac{\kappa_T}{\kappa_s} \sim O(10^2) \qquad (20b)$$

as expected. However, with Eq. (20a), Eq. (18d) has only one admissible root:

$$R_\rho(\mathrm{cr}) = \frac{\kappa_s}{\kappa_T} \sim 10^{-2}, \qquad 10^{-2} \leq R_\rho \leq 1. \qquad (20c)$$

Weak turbulence allows a salt finger range much wider than what is observed [Eq. (18a)].

c. Strong turbulence

Next, we consider a regime opposite to the one in section 6b, namely when molecular effects are negligible. In such a case, we must have

$$\tau_\theta = \tau_S, \qquad \tau_{pS} = \tau_{p\theta}, \tag{21a}$$

which considerably reduces the problem. To discuss $\tau_{s\theta}$, consider the correlation C:

$$C = \overline{T''s''}(\overline{T''}^2)^{-1/2}(\overline{s''}^2)^{-1/2}. \tag{21b}$$

Using Eqs. (8), (9), and (11), Eq. (21b) can be rewritten as

$$\tau_{s\theta} = \tau_s(K_s/K_h)^{1/2}(1 + K_s/K_h)^{-1}C. \tag{21c}$$

Using (21c) in (17a), the latter becomes a quadratic equation in $(K_h/K_s)^{1/2}$ with only one physical root. Since the maximum value of C is unity, such solution is $K_h = K_s$. This is better than (20c) but still not correct since the NATRE data show that $K_s = 1.6K_h$. Furthermore, once $K_s = K_h$ is substituted in (21c) and (18d), it gives

$$\tau_{s\theta}(\max) = \frac{1}{2}\tau_s, \qquad R_\rho(\mathrm{cr}) = 1. \tag{21d}$$

Contrary to the weak turbulence case (20c) that allows too wide a margin for salt fingers, this model has the opposite problem, it allows salt fingers only for $R_\rho = 1$, which contradicts (18a). Thus, even if we know how to compute τ_θ and $\tau_{p\theta}$, we could not use (21d) and we must search for a new model for $\tau_{s\theta}$.

d. Moderate turbulence

Since we do not have a theory capable of encompassing both weak and strong regimes, we must search for a compromise. We suggest the following: we adopt (21a) even in the case of moderate turbulence but not (21d), which we discuss last. To determine τ_θ and $\tau_{p\theta}$, we proceed as follows. Using the T-variance spectrum $E_T(k) = \mathrm{Ba}\epsilon^{-1/3}\chi_T k^{-5/3}$, where Ba is the Batchelor constant, Eq. (19a) gives

$$\frac{\tau_\theta}{\tau} = \frac{\mathrm{Ba}}{\mathrm{Ko}} = \sigma_t = 0.72, \tag{22a}$$

where we have used $\tau = 3\mathrm{Ko}(k_0^2\epsilon)^{-1/3}$. Next, in the limit of strong turbulence and with a Kolmogorov spectrum for $E(k)$, Eq. (19c) gives $\nu_d(k) = (3/20\mathrm{Ko}^3)^{1/2}\epsilon^{1/3}k^{-4/3}$. In the strong limit, Eq. (19d) gives $\chi_d = b^{-1}\nu_d$. If we use the spectrum $J(k) \sim k^{-n}$ with $n = 7/3$, as suggested by numerical simulations and two-point closure models (CD97), Eq. (19b) then yields

$$\frac{\tau}{\tau_{p\theta}} = \left(\frac{27}{5}\mathrm{Ko}^3\right)^{1/2}(1 + \sigma_t^{-1}), \qquad \sigma_t = b = 0.72. \tag{22b}$$

Thus, we have determined four of the needed timescales. As for $\pi_2(\equiv\tau_{s\theta}/\tau)$, we use (21a) in Eq. (18d) but treat π_2 as a free variable. In Fig. 1 we plot R_ρ(cr) versus π_2. One branch corresponds to salt finger while the symmetric one corresponds to diffusive convection. One can see that for a range of salt fingers to exist, $\tau_{s\theta} < \tau_{s\theta}(\max)$. In particular, if we decrease π_2 by 10%, $\tau_{s\theta}(\max)/\tau = \tau_s/\tau = 0.36$, to $\tau_{s\theta}/\tau = 1/3$, we obtain

$$R_\rho(\mathrm{cr}) = 0.62, \qquad 0.62 \leq R_\rho \leq 1, \tag{22c}$$

which is close to (18a). The complete model for the π_s is therefore

$$\pi_1 = \frac{\tau_{ps}}{\tau} = \pi_4 = \frac{\tau_{p\theta}}{\tau} = \left(\frac{27}{5}\mathrm{Ko}^3\right)^{-1/2}(1 + \sigma_t^{-1})^{-1},$$

$$\pi_2 = \frac{\tau_{s\theta}}{\tau} = \frac{1}{3}$$

$$\pi_3 = \frac{\tau_s}{\tau} = \pi_5 = \frac{\tau_\theta}{\tau} = \sigma_t = 0.72. \qquad (22d)$$

7. The critical Ri

In analogy with R_ρ(cr), there is also an Ri^T(cr) above which the effect of stable stratification is stronger than the mixing due to shear. As discussed in Part I, when $R_\rho = 0$ we have $\mathrm{Ri}^T(\mathrm{cr}) \sim O(1)$. How is Ri^T (cr) affected by $R_\rho \neq 0$? Since SF and DC add destabilizing agents, one expects that, in the presence of double diffusion, Ri^T(cr) is larger than without it. As in the case of R_ρ(cr), we obtain Ri^T(cr) by taking the $E \to 0$ limit of (16c). The problem can be treated analytically. Substituting the expressions for $S_{h,\,s}$ from (13b,c), a relatively lengthy algebra leads to the following result:

$$\mathrm{Ri}^T(\mathrm{cr}) = f(R_\rho). \quad (23a)$$

The explicit form of the function $f(R_\rho)$ is given in appendix C. The result is shown in Fig. 2 where we plot iso-contours of S_h beginning with $S_h = 0$ below which there is "*no mixing*"; that is, the $S_h = 0$ curve depicts the function

$$\mathrm{Ri}^T(\mathrm{cr}) \equiv N^2\Sigma^{-2}|_{\mathrm{cr}}. \quad (23b)$$

In the absence of double diffusion $R_\rho = 0$, one observes that $\mathrm{Ri}^T(\mathrm{cr}) \approx 1$, as suggested by Munk (1966). In the presence of double-diffusion and when R_ρ is positive, the value of Ri^T(cr) increases rather slowly at first with R_ρ and then steepens, the asymptote occurring at $R_\rho(\mathrm{cr}) = 0.62$. Since mixing is now enhanced by double diffusion, the overall mixing lives longer, the maximum extent being given by the value of Ri^T(cr). An interesting feature of Fig. 2 is the difference that occurs above and below R_ρ(cr). In the upper curves, where $R_\rho > R_\rho(\mathrm{cr})$, *at fixed* R_ρ, in going from right (small shear) to left (large shear) on the horizontal axis, *the diffusivities* (S_h) *decrease as shear increases.* In the lower region, where $R_\rho < R_\rho(\mathrm{cr})$, at a fixed R_ρ, the opposite occurs, in going from right to left, *the diffusivities increase as the shear increases.* In the last case, when shear is "constructive," mixing is governed mostly by a wave regime (symbol WR) rather than by double diffusion (SF for salt fingers). In the WR regime, we follow Munk's (1966, 1981) suggestion that "the internal wave shear is associated with Richardson numbers of order unity," $\mathrm{Ri}^T \sim \mathrm{Ri}^T(\mathrm{cr}) \sim O(1)$. However, because of double diffusion, Ri^T(cr) is no longer a constant but a function of R_ρ. We shall therefore take

$$\mathrm{Ri}^T = c\mathrm{Ri}^T(\mathrm{cr}) = cf(R_\rho), \quad (23c)$$

where c is a constant of order unity. The sensitivity of the results to the parameter c is exhibited in Fig. 7b.

8. Internal wave field

Below the ML, the shear generated by the external wind is too weak to generate the observed mixing (Ledwell et al. 1993, 1998). On the other hand, a random superposition of internal waves may give rise to a finite probability that local values of Ri fall well below the critical value, for example, $\mathrm{Ri}^T < 1/4$ (Desaubies and Smith 1982). Nonlinear wave interactions have been extensively studied (McComas and Müller 1981; Henyey et al. 1986; Moum and Osborn 1986; Gregg 1989; Polzin et al. 1995; Kunze and Sanford 1996; Gregg et al. 1996; Polzin 1996; Toole 1998; Sun and Kunze 1999a,b; D'Asaro and Lien 2000a,b). In particular, Polzin (1996) has analyzed the dissipation rate ϵ resulting from NATRE data and concluded that the WKB model of Kunze et al. (1990) provides an "effective parameterization of ϵ for a broad range of variability in the background." However, since OGCM do not resolve the pertinent scales, such a model cannot be employed here. Analyzing

several of the suggested models for the ϵ versus N relations, Polzin et al. (1995) concluded that the scaling $\epsilon \sim N^{3/2}$ is not consistent with the data while $\epsilon \sim N^2$ is (their Fig. 4). Using Sargasso Sea data, Kunze and Sanford (1996, KS96) suggest what they call the Gregg–Henyey–Polzin parameterization (cgs units, A is dimensionless):

$$\frac{\epsilon}{N^2} = 0.288A, \qquad A \equiv \frac{\langle V_z^2\rangle^2}{\langle V_z^2\rangle_{\mathrm{GM}}^2} f(R_\omega),$$

$$R_\omega = \langle V_z^2\rangle N^{-2}\xi_z^{-2}. \qquad (23d)$$

Here, $\langle V_z^2\rangle$ is the shear variance referred to the GM background (Garrett and Munk 1975, hereafter GM) and R_ω is the shear to strain (ξ_z) ratio which for GM is 3. The explicit form of $f(R_\omega)$ is given by Eq. (5) of KS96 where Fig. 5 shows that over the entire depth of the ocean, even with $f(R_\omega) = 1$, A varies at most by a factor of ~ 2 in the stratified interior (Polzin et al. 1995; Kunze and Sanford 1996; Gregg et al. 1996; Polzin 1996; Toole 1998).

However, near rough topography, A changes by two to three orders of magnitude (Polzin et al. 1997; Kunze and Toole 1997). Thus, through the presence of ϵ, the present model can account for the different stirring mechanisms that occur in different parts of the ocean, a flexibility that is required for there is no universal stirring mechanism. Moreover, since the diffusivities depend on the efficiency Γ_α, which are also not constant, one needs a turbulence model to compute them.

9. The full model

The fluxes entering Eqs. (2a–c) for the resolved fields are given by Eqs. (2d) and the diffusivities K_α are given by Eqs. (4b). The structure functions S_α are given by Eqs. (13)–(15) and the variable $(\tau N)^2$ is obtained by solving the algebraic relation (16c). The dimensionless variables y, n, and c entering the S_α are then known functions of the large-scale fields. The above procedure is valid both in the ML and below it. As for the dissipation ϵ, one must use different treatments in the ML and below it.

The distinction between the two regimes is made on the basis of the value of $\mathrm{Ri}^T(\text{resolved}) \equiv N^2\Sigma^{-2}$ [see Eq. (3a)]. We use the ML model when $\mathrm{Ri}^T(\text{resolved}) \leq \mathrm{Ri}^T(\text{cr})$. Since the latter is ≥ 1, what is referred to as ML actually includes part of the upper thermocline.

a. Mixed layer

One may adopt the Kolmogorov-type law

$$\epsilon = E^{3/2}\Lambda^{-1} = 8\Lambda^2\tau^{-3}, \qquad (24a)$$

where τ is given by solving (16c). Equation (24a) requires a model for the length scale Λ. Using a two-point closure Cheng and Canuto (1994, CC94) derived an expression for Λ [Eqs. (38) of CC94], which we found to be well represented by the empirical relations (Blackadar 1962; Deardorff 1980):

$$\Lambda = 2^{-3/2}B_1 l, \qquad l = \min\left(\frac{1}{2}\frac{q}{N}, l_1\right),$$

$$l_1 = \kappa z l_0(l_0 + \kappa z)^{-1}, \qquad (24b)$$

which are easier to employ than Eq. (38) of CC94. Here, $q^2 = E$, $\kappa = 0.4$ is the von Kármán constant and $B_1 = 16.6$. In the present case $l_0 = 0.17H$, where H is the mixed layer depth determined by the relation $g[\rho(H) - \rho(\text{surface})]\rho(H)^{-1} = 3 \times 10^{-4}$ m s^{-2}. Other authors (Burchard and Bolding 2001) have employed a differential equation for ϵ.

b. Below the mixed layer

On the one hand, Eq. (24a) does not seem appropriate because it is hard to define a meaningful mixing length Λ, while on

the other hand use of a differential equation for ϵ led to underpredicting ϵ (Burchard et al. 1998), a situation that was remedied by a cutoff in E. D'Asaro and Lien (2000a,b) point out that there is a more basic conceptual problem since the E and ϵ equations, especially the latter, do not naturally account for a basic ingredient of stably stratified flows, the existence of internal waves. Since we arrived at the same conclusion, we decided to consider ϵ as an input function that may be due to internal waves or to more complex processes, as discussed in section 8.

10. Comparison with previous models

Since the Osborn–Cox (1972) and the Osborn (1980) models (called OC models) have been widely used to translate measurements into diffusivities (Davis 1994a,b), it is important to compare ours with the OC models. The most distinguishing features are 1) the OC models employ production equals dissipation, as we do; 2) the OC models were not intended to describe double diffusive processes, which are the primary subject of this paper; 3) the OC models do not compute the mixing efficiencies Γ, which are assigned values around 0.2 as indicated by a variety of data, whereas this model computes them.

To make the comparison physically transparent, consider the mass diffusivity K_ρ, Eq. (3d). It can be written as (R_f is the flux Richardson number):

$$K_\rho = \Gamma_\rho \epsilon N^{-2}, \qquad \Gamma_\rho = R_f(1 - R_f)^{-1},$$
$$R_f \equiv (K_\rho/K_m)\mathrm{Ri}^{\mathrm{T}}. \qquad (24c)$$

Next, if one writes the heat diffusivity as $K_h = \kappa_T C_T$ (Gregg 1987), where C_T is the Cox number, Γ_ρ can be rewritten as

$$\Gamma_\rho = \kappa_T C_T N^2 \epsilon^{-1}(K_\rho/K_h). \quad (24d)$$

When $K_\rho = K_h$, Eq. (24d) becomes Gregg's Eq. (49). Using (3e), we now have

$$\Gamma^{\mathrm{DD}}{}_\rho = \Gamma^{\mathrm{OCG}}{}_\rho(1 - K_s R_\rho/K_h)(1 - R_\rho)^{-1}, \quad (24e)$$

where DD and OCG stand for double diffusion and Osborn–Cox–Gregg. In salt fingers, $K_s > K_h$ while in diffusive convection $K_h > K_s$ so that we have the relations:

$$\mathrm{SF}: \Gamma^{\mathrm{DD}}{}_\rho < \Gamma^{\mathrm{OCG}}{}_\rho, \qquad \mathrm{DC}: \Gamma^{\mathrm{OCG}}{}_\rho < \Gamma^{\mathrm{DD}}{}_\rho. \quad (24f)$$

The primary focus of most recent work has been to assess the relative contributions of turbulence and wave breaking (McDougall and Ruddick 1992; St. Laurent and Schmitt 1999). The latest model by Walsh and Ruddick (2000, WR00) can be formulated as

$$K_\alpha = K_\alpha(\mathrm{SF}) + K_\alpha(t) \qquad (25a)$$
$$K_h(\mathrm{SF}) = \gamma_f K_s(\mathrm{SF}) R_\rho, \qquad K_h(t) = K_s(t), \qquad (25b)$$

where γ_f is the heat-to-salt flux ratio and the letter t stands for turbulence. In Eq. (25b), γ_f is taken from the linear stability analysis (Stern 1975; Kunze 1987; Schmitt 1994) while turbulence yields identical heat and salt diffusivities.

In terms of the model presented in this paper, Eqs. (25) are equivalent to summing the weak and the strong turbulence models discussed earlier. Our model does not impose such a separation and computes γ_f from the full nonlinear problem (Fig. 6). The rationale behind our model is to try to represent the effects of both processes (double diffusion and turbulence) averaged together over space and time. Our view is that, although locally and temporarily there are sometimes salt fingers growing in such a way as to approximate the weak turbulence model as well as laboratory experiments without shear and at other times a random superposition of internal waves may produce so strong a shear that the mixing is well described by a strong regime $K_h = K_s$, neither of these situations is either ubiquitous or permanent. Rather, fingers form and grow for a while but they are disrupted by temporary bursts of high shear that subside and allow the fingers to form and grow again, the two processes eventually reaching equilibrium. The diffusivities K_h and K_s produced by salt fingering, internal wave shear mixing, and the interaction of the two have spatial and temporal scales larger than those of the two

separate processes. Whereas in the previous approaches (St. Laurent and Schmitt 1999; Walsh and Ruddick 2000), the prevalence of salt fingers versus strong turbulence must be computed at each point from the microstructure data, our approach (intended for use in OGCMs where such small-scale information is not available), determines the balance between salt fingering and shear mixing using the large-scale R_ρ. The variation in the relative strengths of the two phenomena at different locations is attributed to the variation in R_ρ.

As for the implementation in OGCM, three approaches were used to treat mixing below the ML. One treats the K_α as adjustable background diffusivities, for example in the NCAR OGCM (Large et al. 1997) K_m = 16.7 cm^2 s^{-1} and $K_s = K_h$ = 0.5 cm^2 s^{-1} while other authors (e.g., Merryfield et al. 1999) use a different set of values. It should be remarked that the above K_m is much larger than one provided by this model (Fig. 8) and so are the values of $K_{h,s}$ compared with 0.07 of Polzin et al. (1995, Fig. 3), 0.1 of Kunze and Sanford (1996, Fig. 5), and the NATRE data (Figs. 9 and 10). Zhang et al. (1998, hereafter ZSH) and Merryfield et al. (1999, hereafter MGH) used model (25) for heat and salt in the form

$$K = K[R_\rho, R_\rho(\text{cr})] + K(\text{waves}). \quad (26a)$$

The first term was taken from the phenomenological models of Schmitt (1981), Fedorov (1988), and Kelley (1984, 1990) and R_ρ(cr) = 0.64 (section 5). As for the second term in (26a), two models have been adopted both of which are independent of R_ρ:

$$K^{\text{ZSH}}(\text{waves}) = K_\infty = \text{const}, \qquad K^{\text{MHG}}(\text{waves}) = a_0 N^{-1}. \quad (26b)$$

In the present model the internal wave contribution depends on R_ρ since schematically

$$K(\text{waves}) = K(\text{Ri}^T, R_\rho, \epsilon) = K(c\text{Ri}^T_{\text{cr}}, R_\rho, \epsilon) = K(R_\rho, \epsilon). \quad (26c)$$

11. Turbulent diffusivities: General properties

Figures 3–4 exhibit the dimensionless structure functions $S_{h,s}$ versus stable Ri^T for salt fingers and diffusive convection. Consider first the case of salt fingers. At a fixed Ri^T, the structure function increases as R_ρ increases. This behavior is physically understandable since the instability is generated by salt and the stronger the source, the larger the diffusivity. Next, consider the dependence on Ri^T and in particular the value of Ri^T(cr) above which turbulent mixing ceases to exist as indicated by the vanishing of the S's. For R_ρ = 0 (lowest curve, no salt instabilities), Ri^T(cr) ~ O(1), as found in Part I. As salt instabilities begin to appear and $R_\rho > 0$, the value of Ri(cr) becomes increasingly larger implying that turbulent mixing can exist longer than without salt instability processes. At $R_\rho = R_\rho$(cr), the value of Ri^T(cr) become exceedingly large, see Fig. 2. For values of $R_\rho > R_\rho$(cr), there is no longer an Ri^T(cr) since the structure functions no longer vanish for any Ri^T. This implies that even without shear Ri$^T \to \infty$, there is finite mixing due to the chaotic nature of the salt instabilities themselves. We notice that below R_ρ(cr), the *larger* the shear (Ri$^T \to 0$), the *larger* the diffusivities. In other words, both salt and shear contribute to the instability. Above R_ρ(cr), the situation is reversed, the larger the shear (Ri$^T \to$ 0), the smaller the diffusivity, which implies that shear and salt fingers interfere. Next, consider the DC cases. At a given Ri^T, as R_ρ increases, the structure function decreases; just the opposite of the SF case. This is in accordance with the fact that in this case salt acts as a sink of mixing (which in turn is caused by an unstable temperature gradient), and thus, the stronger the sink, the lower the level of mixing, a circumstance that is reflected in the decrease of the diffusivity. As for the effect of shear, we notice that here too, above R_ρ(cr), the larger the shear, the larger the diffusivities while the opposite occurs for values of R_ρ larger than that critical value. Finally, we recall that Ri$^T > 0$ corresponds to dynamical stability while Ri$^T < 0$ corresponds to dynamical instability. Understandably, the DS cases correspond to the lowest diffusivity because both salt and temperature gradients are stabilizing. The only source of instability is shear and thus turbulent mixing dies when stratification is too strong. In the DU side, the opposite occurs in the sense that both T and S are unstable and the resulting diffusivities are the largest. In Figs. 5a–c we plot the ratios K_m/K_h and K_s/K_h, which show that K_h and K_s are indeed different. In stable salt fingers, Fig. 5b, K_s is larger than K_h in accord with measured data.

The stable $R_\rho = -1$ case shown in Fig. 5c has been studied with a 2D numerical simulation by Merryfield et al. (1998, Fig. 3b). The results of Fig. 5c are only valid in the regime Re $\gg 1$ where they agree, as expected, with the 2D results (above the dotted lines in their fig. 3b). Intermediate values of Re correspond to a region in which molecular effects are still relevant and one must therefore employ Eqs. (20c) for the π's. It is easy to see that the present model yields $K_h/K_s = 4$ for Fr $\approx$ 28, which agrees pretty well with the corresponding values in Fig. 3b of the 2D simulation (we recall that our $x = 4\mathrm{Fr}^{-2}$).

In Fig. 6 we plot the heat-to-salt flux ratio $(K_h/K_s)R^{-1}_\rho$. Since $R_\rho(\mathrm{cr}) = 0.62$ and since for $R_\rho < R_\rho(\mathrm{cr})$, we have a wave dominated regime (WR), while for $R_\rho > R_\rho(\mathrm{cr})$ we have salt fingers (SF), we notice that in the SF region, the model results agree with the reported data (see Figs. 5b and 10 of St. Laurent and Schmitt 1999). In the wave region (WR), the presence of the additional mixing due to shear increases both K_h and K_s, making their ratio become closer to unity than in the SF regime. The behavior in Fig. 6 is in agreement with the model of Walsh and Ruddick (2000, Fig. 2).

In Fig. 7a we plot $\Gamma_h = K_h N^2 \epsilon^{-1}$ versus $R^{-1}_\rho - 1$ for different values of stable Ri^T. The lowest curve is for $\mathrm{Ri}^T = 0.1$, while the upper curve is for $\mathrm{Ri}^T = 20$. As expected from Fig. 2, in the SF regime ($R_\rho > 0.62$), the larger the shear, the lower the value of Γ_h. The largest Ri^T curve corresponds to the points to the extreme right of Fig. 2 and the corresponding $R_\rho(\mathrm{cr}) = 0.62$. As we consider increasingly smaller values of Ri^T, we are sliding down the dividing line in Fig. 2, which corresponds to smaller $R_\rho(\mathrm{cr})$ and this moves the last point of the curves in Fig. 7a to the right. This general trend is in keeping with the NATRE results of Fig. 9 of St. Laurent and Schmitt (1999, hereafter SLS) where the smaller the value of Ri^T, the wider the range of R_ρ allowed. In particular, from Fig. 9f of SLS we see that for $Ri^T > 5$, the range of allowed R_ρ is $0.5 \leq R_\rho \leq 1$, in agreement with both Figs. 2 and 7a. We also notice from Figs. 9a–f of SLS that the larger the Ri^T, the larger the Γ_h, a feature that is also reproduced in our Fig. 7a. In Fig. 7b we exhibit Γ_h versus stable Ri^T for different R_ρ. The two lines A and B correspond to different choices of c in Eq. (23c): $A(c = 0.85)$ and $B(c = 1)$. One can see that for a given R_ρ, the choice of c does not greatly influence the resulting value of Γ_h. In Fig. 7c we exhibit Γ_ρ versus R_ρ for different stable Ri^T. The Osborn–Cox model employs $\Gamma_\rho = 0.2$, which the present model reproduces in the WR regime.

12. Testing the model without an OGCM

Though the ultimate goal is to employ the new diffusivities in an OGCM, it would be very helpful and less affected by the unavoidable complexities of any OGCM, if one could use the NATRE data to test the model directly. This is indeed possible. In the deep ocean, the present model yields diffusivities (1b) that depend on R_ρ, N, and ϵ. Due to the location of the NATRE experiments, ϵ can be modeled with (23d). Thus, the comparison with NATRE data can be carried out without running an OGCM: using R_ρ (data) in our model expressions, one obtains K_α (model), which is then compared with K_α (data). Some of the results are presented in Figs. 9a,b. We extracted the errors in R_ρ and K_h from St. Laurent and Schmitt (1999) and thus both data and model results are shown with error bars. The K_α are sensitive to π_2 and we verified that a slightly larger π_2 would improve the agreement. The procedure faces a practical difficulty since NATRE data fall within a small interval of R_ρ that cluster around $R_\rho(\mathrm{cr})$. As one can see from Fig. 7a, in this small interval Γ_h is a steep function of R_ρ and a small error in R_ρ can give quite different Γ_h.

13. Testing the model with an OGCM

We employed a 3D global ocean model, the NCAR CSM Ocean Model produced by the University Corporation for Research, National Center for Atmospheric Research, Climate and Global Dynamics Division. We used the stand-alone 3° × 3° configuration with 25 levels (Large et al. 1997). Details can be found in Part I.

In Figs. 10a–d, we present momentum, heat, salt, mass, and concentration diffusivities versus the NATRE data [diamonds from SLS99 and triangles from Ledwell et al. (1998); Watson and Ledwell (2000)]. In Fig. 10d, the triangle to the left corresponds to the first six months of the experiment while the one to the right corresponds to the next two years of measurements. The error bars of the NATRE data are also shown. The agreement between the model results and the data is satisfactory. In Fig. 11, we show the density ratio R versus z using the same NATRE data.

14. Global ocean results

Using the new model for the K_s, we obtain the results presented in Figs. 12–18. In Figs. 12–15, the Levitus et al. (1994) data are represented by the full line. We ran the code with both the K parameter parameterization (KPP) model ($K_h = K_s$ and adjustable background diffusivities; Large et al. 1997) and our model. The diamonds correspond to the KPP model and the asterisks correspond to the present model. In Fig. 12 we plot the global average temperature. The new model yields a closer fit to Levitus data than previous models especially in the first 1 km. As for the salinity (Fig. 13), the new model improves the correspondence with Levitus data in the upper kilometer. In the Arctic Ocean (Fig. 14), the temperature profile is improved versus the KPP model; as for the salinity (Fig. 15), the new model brings about a considerable improvement over the KPP model in the ML where the KPP model indicated a freshening of the water masses. In Figs. 16, we present the North Atlantic overturning streamfunction (in Sv) with double diffusion (a) and without it (b). At 24°N, the presence of double diffusion yields a better fit to the measured values 16 ± 5 Sv and 17 ± 4 Sv (Roemmich and Wunsch 1985; Macdonald and Wunsch 1996). In Fig. 17, we show the polar heat transport in the North Atlantic (a), Indo–Pacific Ocean (b) and global ocean (c). The data, the symbols, and the error bars are from Macdonald and Wunsch (1996). As one can notice, while the agreement is generally acceptable, the presence of double diffusion has lowered the polar heat transport, a fact noticed by previous authors. To be more realistic, one must change the salinity boundary conditions from “restoring,” as used in part in the NCAR–CSM ocean model, to “natural” (Huang 1993) so as to ensure that there is no salt flux across the air–sea interface, as the physics of the problem requires. Jiang et al. (1999) used these boundary conditions, together with an updated set of $E - P$ values, and showed that the heat transport increases by 23% while at 24°N the thermohaline circulation increases from 12 Sv to 27 Sv. These values correspond to the case of a horizontal diffusivity; if the latter is substituted with the Gent–McWilliams model, the 27 Sv value decreases to 21 Sv, which will get closer to the measured values once the effect of double diffusion is included. Finally, in Fig. 18, we present the model results for the freshwater budgets, which were computed as in Danabasoglu and McWilliams (1994). Generally, the new model gives similar results to KPP, but the magnitude of the transport in the North Atlantic has been noticeably reduced.

15. Discussion

Given the relevance of double-diffusion processes in the ocean, several authors have studied the phenomenon and its implications on ocean dynamics (Gargett and Holloway 1992; Zhang et al. 1998; Merryfield et al. 1999; Zhang and Schimtt 2000). While laboratory data on salt fingers (SF) are quite extensive, their utilization in an OGCM is not straightforward since oceanic SF occur in a complex environment where, for example, there are wave breaking processes. To account for both processes is a difficult task and different authors have used different approaches. The most recent model, Eqs. (25), is based on the following assumptions:

1. SF (salt fingers) and WR (wave regime, called turbulence) exist simultaneously,
2. SF and WR dominate in different regions separated by a critical R_ρ(cr) below which WR dominate and above which SF dominate,
3. the expression for the SF diffusivities is taken from phenomenological models (e.g., Schmitt 1981; Fedorov 1988; Kelly 1984, 1990),
4. the value of R_ρ(cr) is empirically determined to be 0.64,
5. the term in (26a) contributed by wave braking has been taken alternatively as a constant or a function of the type a/N, Eq. (26b).

The present model is not based on the above assumptions and double diffusion and stirring by waves are treated within the same formalism, which also yields the value of R_ρ(cr). Interestingly enough, the results of the present model shown in Fig. 6 are very close to those of Fig. 2 of Walsh and Ruddick (2000). This is however more than a theoretical validation of model (25) since the latter is only valid for salt fingers whereas the present model encompasses all double diffusion processes. In addition, the combination SF + WR is not the only one in the ocean since, as discussed earlier, there is a variety of stirring sources in addition to wave breaking.

At a more basic level, there is a methodological difference. We have adopted an Osborn–Cox-like approach based on the dynamic equations, which we enlarged to include all the dynamic equations relevant to the presence of velocity, temperature, and salinity fields. The only methodology capable of doing so is the Reynolds stress model.

We have derived the expressions for the diffusivities of momentum, heat, and salt as a function of the Richardson number Ri^T, density ratio R_ρ, Brunt–Väisälä frequency N, and rate of dissipation of turbulent kinetic energy ϵ. The model encompasses salt fingers, diffusive convection, and doubly stable and doubly unstable cases as well as shear. The latter, though of different origin at different depths, is always present in the ocean. Within the mixed layer, it is due to external winds while in the ocean interior, it may be due to a variety of sources. The model is valid in both the ML and below it in the sense that the functional dependence of the diffusivities on the variables Ri^T, R_ρ, N, and ϵ is the same throughout the vertical extent of the ocean. What is different between the ML and thermocline (and below it) is the modeling of Ri^T and ϵ.

16. Future improvements of the model

The major difficulty in constructing this model was the evaluation of the dissipation timescales. Since the presence of salt fingers is an indication that molecular effects are important, one is called upon to construct a model that is atypical since most turbulence models assume negligible molecular effects. The weak and strong turbulence models presented earlier represent two extremes and neither one is representative of ocean mixing. What is required is a model that encompasses both limits but such a model is still not available. In our approach, the molecular/turbulence interface is represented by a single variable, the correlation timescale $\tau_{s\theta}$ whose value from the turbulence model was slightly too large. A 10% decrease was sufficient to reproduce the correct value of R_ρ(cr). The theoretical challenge is how to compute $\tau_{s\theta}$ from a two-point closure model.

The present model is local since Eqs. (5)–(11) do not contain the third-order moments (TOM), for example, $\overline{u_i'' T''^2}$, that would appear in the left-hand side of Eq. (7). The presence of nonlocal terms would change the heat flux expression in (2d) to

$$\overline{w''T''} = -K_h\left(\frac{\partial T}{\partial z} + \Gamma\right), \qquad (27a)$$

where Γ, known as the countergradient term, is a function of the TOMs. Since a new, algebraic expression for the TOMs has recently been derived (Canuto et al. 1994; Canuto et al. 2001a), the present model can be made nonlocal.

Finally, the treatment of wave–turbulence interaction can also be improved. In fact, one may further split any turbulent variable Φ'' as

$$\Phi'' = \Phi''_t + \Phi''_w, \qquad (27b)$$

where the subscripts t and w stand for turbulence and waves. This has already been done in the atmospheric context (Finnigan and Einaudi 1981) and it could also be applied here with an unavoidable increase in the number of equations to solve. However, it may be an effort worth pursuing because of the new physical insight one may gain from it.

Acknowledgments

The authors would like to thank three referees who greatly helped improve the manuscript. Dr. G. Holloway suggested the test discussed in section 12.

REFERENCES

Adcroft A., J. R. Scott, and J. Marotzke, 2001: Impact of geothermal heating on the global ocean circulation. *Geophys. Res. Lett*, **28**, 1735–1738. Find this article online

Armi L., and R. C. Millard Jr., 1976: The bottom boundary layer of the deep ocean. *J. Geophys. Res*, **81**, 4983–4990. Find this article online

Bell T. H. Jr., 1975: Topographically generated internal waves in the open ocean. *J. Geophys. Res*, **80**, 320–327. Find this article online

Blackadar A. K., 1962: The vertical distribution of wind and turbulent exchange in neutral atmosphere. *J. Geophys. Res*, **67**, 3095–3102. Find this article online

Burchard H., and K. Bolding, 2001: Comparative analysis of four second moment turbulence closure models for the oceanic mixed layer. *J. Phys. Oceanogr*, **31**, 1943–1968. Find this article online

Burchard H., and E. Deleersnijder, 2001: Stability of algebraic non-equilibrium second-moment turbulence closure models. *Ocean Modelling*, **3,** 33–50.

Burchard H., O. Peterson, and T. P. Rippeth, 1998: Comparing the performance of the Mellor–Yamada and the K-ϵ two equation turbulence models. *J. Geophys. Res*, **103**, 10543–10554. Find this article online

Canuto V. M., and M. S. Dubovikov, 1996a: A dynamical model for turbulence: I. General formalism. *Phys. Fluids*, **8**, 571–586. Find this article online

Canuto V. M., and M. S. Dubovikov, 1996b: A dynamical model for turbulence: II. Shear-driven flows. *Phys. Fluids*, **8**, 587–598. Find this article online

Canuto V. M., and M. S. Dubovikov, 1997: A dynamical model for turbulence: IV. Buoyancy driven flows. *Phys. Fluids*, **9**, 2118–2131. Find this article online

Canuto V. M., F. Minotti, C. Ronchi, R. M. Ypma, and O. Zeman, 1994: Second-order closure PBL model with new third-order moments. Comparison with LES data. *J. Atmos. Sci*, **51**, 1605–1618. Find this article online

Canuto V. M., Y. Cheng, and A. Howard, 2001a: New third-order moments for the CBL. *J. Atmos. Sci*, **58**, 1169–1172. Find this article online

Canuto V. M., A. Howard, Y. Cheng, and M. S. Dubovikov, 2001b: Ocean Turbulence. Part I: One-point closure model. Momentum and heat vertical diffusivities. *J. Phys. Oceanogr*, **31**, 1413–1426. Find this article online

Cheng Y., and V. M. Canuto, 1994: Stably stratified shear turbulence: A new model for the energy dissipation length scale. *J. Atmos. Sci*, **51**, 2384–2396. Find this article online

Danabasoglu G., and J. C. McWilliams, 1995: Sensitivity of the global ocean circulation to parameterizations of mesoscale tracer transport. *J. Climate*, **8**, 2967–2987. Find this article online

D'Asaro E. A., and R.-C. Lien, 2000a: Lagrangian measurements of waves and turbulence in stratified flows. *J. Phys. Oceanogr*, **30**, 641–655. Find this article online

D'Asaro E. A., and R.-C. Lien, 2000b: The wave–turbulence transition for stratified flows. *J. Phys. Oceanogr*, **30**, 1669–1678. Find this article online

Davis R. E., 1994a: Diapycnal mixing in the ocean: Equations for the large scale budgets. *J. Phys. Oceanogr*, **24**, 777–800. Find this article online

Davis R. E., 1994b: Diapycnal mixing in the ocean: The Osborn–Cox Model. *J. Phys. Oceanogr*, **24**, 2560–2576. Find this article online

Deardorff J. W., 1980: Stratocumulus-capped mixed layer derived from a 3D model. *Bound.-Layer Meteor*, **18**, 495–502. Find this article online

Desaubies Y., and W. K. Smith, 1982: Statistics of Richardson number and instabilities in oceanic internal waves. *J. Phys. Oceanogr*, **12**, 1245–1259. Find this article online

Egbert G. D., and R. D. Ray, 2000: Significant dissipation of tidal energy in the deep ocean inferred from satellite data. *Nature*, **405**, 775–778. Find this article online

Fedorov K. N., 1988: Layer thickness and effective diffusivities in “diffusive” thermohaline convection in the ocean. *Small Scale Turbulence and Mixing in the Ocean*, J. Nihoul and B. Jamart, Eds., Vol. 46, Elsevier, 471–480.

Finnigan J. J., and F. Einaudi, 1981: The interaction between an internal gravity wave and the planetary boundary layer. Part II: Effect of the wave on the turbulence structure. *Quart. J. Roy. Meteor. Soc*, **107**, 807–832. Find this article online

Gargett A. E., and G. Holloway, 1992: Sensitivity of the GFDL ocean model to different diffusivities for heat and salt. *J. Phys. Oceanogr*, **22**, 1158–1177. Find this article online

Gargett A. E., and B. Ferron, 1996: The effect of differential vertical diffusion of T and S in a box model of thermohaline circulation. *J. Mar. Res*, **54**, 827–866. Find this article online

Garret C. J. R., and W. H. Munk, 1975: Space–time scales of internal waves: A progress report. *J. Geophys. Res*, **80**, 291–297. Find this

article online

Gatski T. B., S. Sarkar, and C. G. Speziale, 1993: *Studies in Turbulence*. Springer Verlag, 602 pp.

Gregg M. C., 1987: Diapycnal mixing: A review. *J. Geophys. Res*, **92**, 5249–5286. Find this article online

Gregg M. C., 1989: Scaling turbulent dissipation in the thermocline. *J. Geophys. Res*, **94**, 9689–9698. Find this article online

Gregg M. C., D. P. Winkel, T. S. Sanford, and H. Peters, 1996: Turbulence produced by internal waves in the oceanic thermocline at mid and low latitudes. *Dyn. Atmos. Oceans*, **24**, 1–14. Find this article online

Henyey F. S., J. Wright, and S. M. Flatte, 1986: Energy and action flow through the internal wave field. An eikonal approximation. *J. Geophys. Res*, **91**, 8487–8495. Find this article online

Huang R. X., 1993: Real freshwater flux as the upper boundary condition for the salinity balance and the thermocline circulation forced by evaporation and precipitation. *J. Phys. Oceanogr*, **23**, 2428–2446. Find this article online

Jayne S. R., and L. C. St. Laurent, 2001: Parameterizing tidal dissipation over rough topography. *Geophys. Res. Lett*, **28**, 811–814. Find this article online

Jiang S., P. H. Stone, and P. Malanotte-Rizzoli, 1999: An assessment of the GFDL ocean model with coarse resolution: Annual-mean climatology. *J. Geophys. Res*, **104**, 25623–25645. Find this article online

Kelley D. E., 1984: Effective diffusivities within oceanic thermohaline staircases. *J. Geophys. Res*, **89**, 10484–10488. Find this article online

Kelley D. E., 1990: Fluxes through diffusive staircases: A new formulation. *J. Geophys. Res*, **95**, 3365–3371. Find this article online

Kunze E., 1987: Limits to growing, finite-length salt fingers: A Richardson number constraint. *J. Mar. Res*, **45**, 533–556. Find this article online

Kunze E., 1990: The evolution of salt fingers in inertial wave shear. *J. Mar. Res*, **48**, 471–504. Find this article online

Kunze E., and T. S. Sanford, 1996: Abyssal mixing: Where it is not. *J. Phys. Oceanogr*, **26**, 2286–2296. Find this article online

Kunze E., and J. M. Toole, 1997: Tidally driven vorticity, diurnal shear and turbulence atop Fieberling Seamount. *J. Phys. Oceanogr*, **27**, 2663–2693. Find this article online

Large W. G., J. C. McWilliams, and S. C. Doney, 1994: Oceanic vertical mixing: A review and a model with non-local boundary layer parameterization. *Rev. Geophys*, **32**, 363–403. Find this article online

Large W. G., G. Danabasoglu, S. C. Doney, and J. C. McWilliams, 1997: Sensitivity to surface forcing and boundary layer mixing in a global ocean model: Annual-mean climatology. *J. Phys. Oceanogr*, **27**, 2418–2447. Find this article online

Ledwell J. R., A. J. Watson, and C. S. Law, 1993: Evidence for slow mixing across the pycnocline from an open ocean tracer-release experiment. *Nature*, **364**, 701–703. Find this article online

Ledwell J. R., A. J. Watson, and C. S. Law, 1998: Mixing of a tracer in the pycnocline. *J. Geophys. Res*, **103**, 21499–21529. Find this article online

Ledwell J. R., E. T. Montgomery, K. L. Polzin, L. St. Laurent, R. W. Schmitt, and J. M. Toole, 2000: Evidence for enhanced mixing over rough topography in the abyssal ocean. *Nature*, **403**, 179–182. Find this article online

Levitus S., and T. P. Boyer, 1994: *World Ocean Atlas 1994*. Vol. 4: *Temperature, NOAA Atlas NESDIS 4*, 129 pp.

Levitus S., R. Burgett, and T. P. Boyer, 1994: *World Ocean Atlas 1994*. Vol. 3: *Salinity, NOAA Atlas NESDIS3*, 99 pp.

McDonald A. M., and C. Wunsch, 1996: An estimate of global ocean circulation and heat fluxes. *Nature*, **382**, 436–439. Find this article online

McComas C. H., and P. Muller, 1981: The dynamic balance of internal waves. *J. Phys. Oceanogr*, **11**, 970–986. Find this article online

McDougall T., and B. Ruddick, 1992: The use of ocean miscrostructure to quantify both turbulent mixing and salt-fingers. *Deep-Sea Res*, **11/12**, 1931–1952. Find this article online

Mellor G. L., and T. Yamada, 1982: Development of a turbulence closure model for geophysical fluid problems. *Rev. Geophys. Space Phys*, **20**, 851–875. Find this article online

Merryfield W. J., G. Holloway, and A. E. Gargett:, 1998: Differential vertical transport of heat and salt by weak stratified turbulence. *Geophys. Res. Lett*, **25**, 2773–2776. Find this article online

Merryfield W. J., G. Holloway, and A. E. Gargett:, 1999: A global ocean model with double diffusive mixing. *J. Phys. Oceanogr*, **29**, 1124–1142. Find this article online

Monin A. S., and A. M. Yaglom, 1971: *Statistical Fluid Mechanics*: *Mechanics of Turbulence* Vol. 1, The MIT Press, 769 pp.

Monin A. S., and A. M. Yaglom, 1975: *Statistical Fluid Mechanics: Mechanics of Turbulence*. Vol. 2, The MIT Press, 874 pp.

Moum J. N., and T. R. Osborn, 1986: Mixing in the main thermocline. *J. Phys. Oceanogr*, **16**, 125–129. Find this article online

Müller P., and N. Xu, 1992: Scattering of oceanic internal gravity waves off random bottom topography. *J. Phys. Oceanogr*, **22**, 474–488. Find this article online

Munk W. H., 1966: Abyssal recipes. *Deep-Sea Res*, **13**, 707–730. Find this article online

Munk W. H., 1981: Internal waves and small scale processes. *Scientific Surveys in Honor of H. Stommel*, B. A. Warren and C. Wunsch, Eds., The MIT Press, 264–291.

Munk W. H., and C. Wunsch, 1998: Abyssal recipes II: Energetics of tidal and wind mixing. *Deep-Sea Res. I*, **45**, 1977–2110. Find this article online

Osborn T. R., 1980: Estimates of the local rate of vertical diffusion from dissipation measurements. *J. Phys. Oceanogr*, **10**, 83–89. Find this article online

Osborn T. R., and C. S. Cox, 1972: Oceanic fine structure. *Geophys. Fluid Dyn*, **3**, 321–345. Find this article online

Polzin K., 1996: Statistics of the Richardson number: Mixing models and fine structure. *J. Phys. Oceanogr*, **26**, 1409–1425. Find this article online

Polzin K., J. M. Toole, and R. W. Schmitt, 1995: Finescale parameterization of turbulent dissipation. *J. Phys. Oceanogr*, **25**, 306–328. Find this article online

Polzin K., J. R. Ledwell, and R. W. Schmitt, 1997: Spatial variability of turbulent mixing in the abyssal ocean. *Science*, **276**, 93–96. Find this article online

Roemmich D., and C. Wunsch, 1985: Two transatlantic sections: Meridional circulation and heat flux in the subtropical North Atlantic Ocean. *Deep-Sea Res*, **32**, 619–664. Find this article online

Schmitt R. W., 1981: Form of the T–S relationship in central waters: Evidence for double diffusive mixing. *J. Phys. Oceanogr*, **11**, 1015–1026. Find this article online

Schmitt R. W., 1994: Double diffusion in oceanography. *Ann. Rev. Fluid Dyn*, **26**, 255–285.

Schmitt R. W., and D. L. Evans, 1978: An estimate of the vertical mixing due to salt fingers based on observations in the North Atlantic central waters. *J. Geophys. Res*, **83**, 2913–2919. Find this article online

St. Laurent L., and R. W. Schmitt, 1999: The contribution of salt fingers to vertical mixing in the NATRE experiment. *J. Phys. Oceanogr*, **29**, 1404–1424. Find this article online

Stern M. E., 1975: *Ocean Circulation Physics*. Academic Press, 246 pp.

Sun H., and E. Kunze, 1999a: Internal wave–wave interactions. Part I: The role of internal wave vertical divergence. *J. Phys. Oceanogr*, **29**, 2886–2904. Find this article online

Sun H., and E. Kunze, 1999b: Internal wave–wave interactions. Part II: Spectral energy transfer and turbulence production. *J. Phys. Oceanogr*, **29**, 2905–2919. Find this article online

Toole J. M., 1998: Turbulent mixing in the ocean. *Ocean Modeling and Parameterization*, E. P. Chassignet and J. Verron, Eds., NATO Science Series, Vol. 516, Kluwer Academic, 171–190.

Walsh D., and B. Ruddick, 2000: Double-diffusion interleaving in the presence of turbulence. The effect of a nonconstant flux ratio. *J. Phys. Oceanogr*, **30**, 2231–2245. Find this article online

Watson A. J., and J. R. Ledwell, 2000: Oceanographic tracer release experiments using SF. *J. Geophys. Res*, **105**, 14325–14337. Find this

article online

Wijfells E. E., R. W. Schmitt, H. L. Bryden, and A. Stigebrandt, 1992: Transport of freshwater by the oceans. *J. Phys. Oceanogr*, **22**, 155–162. Find this article online

Wunsch C., 2000: Moon, tides and climate. *Nature*, **405**, 743–744. Find this article online

Zeman O., and J. L. Lumley, 1982: Modeling salt-fingers structures. *J. Mar. Res*, **40**, 315–330. Find this article online

Zeman O., and J. L. Lumley, 1983: Progress in modeling multilayer salt-fingers structures. *Math. Model*, **4**, 73–85.

Zhang J., and R. Schmitt, 2000: The impact of salt fingering on the thermohaline circulation under mixed boundary conditions. *J. Phys. Oceanogr*, **30**, 1223–1231. Find this article online

Zhang J., R. Schmitt, and R. X. Huang, 1998: Sensitivity of the GFDL ocean model to parameterization of double-diffusion processes. *J. Phys. Oceanogr*, **28**, 589–605. Find this article online

Zhang J., R. Schmitt, and R. X. Huang, 1999: The relative influence of diapycnal mixing and hydrological forcing on the stability of the thermocline circulation. *J. Phys. Oceanogr*, **29**, 1096–1108. Find this article online

---

APPENDIX A

17. Functions in Eqs. (13)–(14)

Using the abbreviated notation:

$$p_{1m} = 1 - p_1, \qquad p_{2m} = 1 - p_2, \qquad p_3 = \frac{5}{2}\pi_1,$$

$$p_4 = \frac{1}{5}\pi_1\pi_3^{-2}, \qquad p_5 = \pi_1\pi_2\pi_3^{-2},$$

$$p_6 = \frac{1}{5}\pi_3^{-1}\pi_2^{-1}\pi_4, \qquad p_7 = 5\pi_2, \qquad p_8 = \frac{5}{2}\pi_4,$$

$$p_9 = \pi_5\pi_4(\pi_3\pi_2)^{-1}, \qquad p_{10} = \pi_2\pi_4\pi_3^{-2},$$

$$p_{11} = \pi_1\pi_3^{-1} \tag{A1}$$

the functions a_k, b_k, and d_k entering Eqs. (13)–(14) are given by

$$\begin{aligned}
a_1 &= p_{11}[12p_9 + 8p_6 - 30p_6p_8 - 5p_6(p_{1m} + 3p_{2m})] \\
a_2 &= [8 - 5(p_{1m} + 3p_{2m})](p_4p_9 + p_6p_{11} - 2p_5p_6) \\
&\quad + 12p_{11}p_9 \\
&\quad - 30(p_3p_4p_9 + p_6p_8p_{11} - p_5p_6p_8 - p_3p_5p_6) \\
a_3 &= p_{10}[8p_4 + 12p_{11} - 30p_3p_4 - 5p_4(p_{1m} + 3p_{2m})] \\
a_4 &= -p_6(8 - 30p_8 - 5p_{1m} - 15p_{2m}) - 12(p_9 + p_{11}) \\
a_5 &= -p_4(8 - 30p_3 - 5p_{1m} - 15p_{2m}) - 12(p_{10} + p_{11})
\end{aligned} \tag{A2}$$

$$b_1 = \pi_1\pi_3^{-2}(\pi_2 - \pi_3), \qquad b_2 = -\pi_1\pi_3^{-1},$$

$$b_3 = 15p_{2m}^2 + 2p_{1m} - 5p_{1m}^2 - 6p_{2m} \qquad b_4 = -6\pi_1\pi_3^{-2},$$

$$b_5 = -6\pi_4\pi_2^{-1}\pi_3^{-1} \qquad b_6 = -\pi_2\pi_4\pi_3^{-2}$$

$$b_7 = \pi_4\pi_2^{-1}\pi_3^{-1}(\pi_2 - \pi_5) \tag{A3}$$

$$\begin{aligned} d_1 &= p_{11}[p_{2m}^2(p_6 + 6p_9) + 2(p_{1m} - 3p_{2m})p_6p_8 \\ &\qquad - p_{1m}^2(p_6 + 2p_9)] \\ d_2 &= (p_{1m}^2 - p_{2m}^2)(2p_5p_6 - p_6p_{11} - p_4p_9) \\ &\quad + 2(p_{1m}^2 - 3p_{2m}^2)(p_5p_6p_7 - p_{11}p_9 - p_{10}p_{11}) \\ &\quad + 2(p_{1m} - 3p_{2m}) \\ &\quad \times (p_3p_4p_9 + p_6p_8p_{11} - p_5p_6p_8 - p_3p_5p_6) \\ d_3 &= p_{10}[p_{2m}^2(p_4 + 6p_{11}) + 2(p_{1m} - 3p_{2m})p_3p_4 \\ &\qquad - p_{1m}^2(p_4 + 2p_{11})] \\ d_4 &= -4p_6p_{11}(2p_6 + 3p_9) \\ d_5 &= 4p_4p_7p_6^2(4 + 3p_7) - 4p_4p_9(3p_{11} + 2p_6) \\ &\quad - 4p_6p_{11}(3p_9 + 3p_{10} + 2p_4 + 2p_6) \\ d_6 &= 4p_4^2p_6p_7(4 + 3p_7) - 4p_4p_9(2p_4 + 3p_{11}) \\ &\quad - 8p_4p_6(p_{10} + p_{11}) - 12p_{10}p_{11}(p_4 + p_6) \\ d_7 &= -4p_4p_{10}(2p_4 + 3p_{11}) \\ d_8 &= p_{1m}^2(2p_9 + 2p_{11} + p_6) - p_{2m}^2(6p_9 + 6p_{11} + p_6) \\ &\quad - 2p_6p_8(p_{1m} - 3p_{2m}) \\ d_9 &= p_{1m}^2(2p_{11} + 2p_{10} + p_4) - p_{2m}^2(6p_{11} + 6p_{10} + p_4) \\ &\quad - 2p_3p_4(p_{1m} - 3p_{2m}) \\ d_{10} &= 8p_6^2 + 4p_6(3p_9 + 7p_{11}) + 24p_9p_{11} \\ d_{11} &= -8p_5p_6(4 + 3p_7) + 4p_4(4p_6 + 7p_9 + 3p_{11}) \\ &\quad + 4p_6(3p_{10} + 7p_{11}) + 24p_{11}(p_9 + p_{10}) \\ d_{12} &= 4p_{10}(7p_4 + 6p_{11}) + 4p_4(2p_4 + 3p_{11}) \\ d_{13} &= 6p_{2m}^2 - 2p_{1m}^2 \qquad d_{14} = -24p_9 - 24p_{11} - 28p_6 \end{aligned}$$

$$d_{15} = -24p_{11} - 24p_{10} - 28p_4. \quad \text{(A4)}$$

APPENDIX B

18. Values of the Constants in Eqs. (13)–(15)

In the present model, the π_s are given by Eqs. (22d):

$$\pi_1 = \pi_4 = 0.08372, \qquad \pi_2 = 1/3, \qquad \pi_3 = \pi_5 = 0.72, \quad \text{(B1)}$$

and

$$p_1 = 0.832, p_2 = 0.545. \quad \text{(B2)}$$

Thus, the p_k, a_k, b_k, and d_k of appendix A take the numerical values:

$$p_3 = 0.2093, \quad p_4 = 0.0323, \quad p_5 = 0.0538,$$
$$p_6 = 0.0698, \quad p_7 = 1.6666, \quad p_8 = 0.2093,$$
$$p_9 = 0.2511, \quad p_{10} = 0.0538,$$
$$p_{11} = 0.1163, \quad \text{(B3)}$$

$$a_1 = 0.3022, \quad a_2 = 0.2986, \quad a_3 = 0.06478,$$
$$a_4 = -3.99459, \quad a_5 = -1.8493, \quad \text{(B4)}$$

$$b_1 = -0.0625, \quad b_2 = -0.1163, \quad b_3 = 0.5702,$$
$$b_4 = -0.9689, \quad b_5 = -2.0930,$$
$$b_6 = -0.0538, \quad b_7 = -0.13488, \quad \text{(B5)}$$

$$d_1 = 0.03201, \quad d_2 = 0.0318,$$
$$d_3 = 0.00686, \quad d_4 = -0.0289,$$
$$d_5 = -0.04272, \quad d_6 = -0.01978,$$
$$d_7 = -0.002875, \quad d_8 = -0.41319,$$
$$d_9 = -0.1912, \quad d_{10} = 1.1773,$$
$$d_{11} = 1.1612, \quad d_{12} = 0.2523,$$
$$d_{13} = 1.1857, \quad d_{14} = -10.7721,$$
$$d_{15} = -4.9871. \quad \text{(B6)}$$

APPENDIX C

19. The Function $f(R_\rho)$, Eq. (23a)

The function $f(R_\rho)$ of Eq. (23a) is given by

$$f(R_\rho) = f_1 f_2^{-1} \tag{C1}$$

$$f_1 = 2a_m(1 - R_\rho) - 5(\pi_4\alpha_2 - \pi_1\alpha_4 R_\rho) - 6\delta_0(1 - R_\rho) \tag{C2}$$

$$f_2 = 6\delta_1(1 - R_\rho) + 5(\pi_4\alpha_1 - \pi_1\alpha_3 R_\rho), \tag{C3}$$

where

$$a_m = a_1 N_0^2 + a_2 N_0 C_0 + a_3 C_0^2$$

$$\alpha_1 = b_1 b_4 C_0^2 + (b_1 b_5 + b_2 b_4) N_0 C_0 + b_2 b_5 N_0^2$$

$$\alpha_2 = b_1 b_3 C_0 + b_2 b_3 N_0$$

$$\alpha_3 = b_4 b_6 C_0^2 + (b_5 b_6 + b_4 b_7) N_0 C_0 + b_5 b_7 N_0^2$$

$$\alpha_4 = b_3 b_6 C_0 + b_3 b_7 N_0$$

$$\delta_0 = d_1 N_0^2 + d_2 N_0 C_0 + d_3 C_0^2$$

$$\delta_1 = d_4 N_0^3 + d_5 C_0 N_0^2 + d_6 N_0 C_0^2 + d_7 C_0^3$$

$$N_0 = -\frac{25}{4}\pi_2\pi_3(1 - R_\rho)^{-1}$$

$$C_0 = \frac{25}{4}\pi_3^2 R_\rho(1 - R_\rho)^{-1}. \tag{C4}$$

Figures

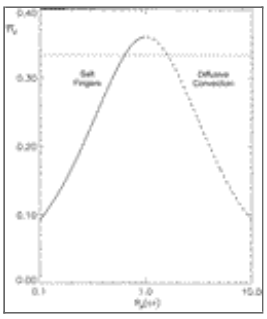

Click on thumbnail for full-sized image.

FIG. 1. The function R_ρ(cr) given by Eqs. (18d) with $\pi_2 = \tau_{s\theta}/\tau$ treated as a free variable. The full line corresponds to salt fingers while the dashed line corresponds to diffusive convection. If we take $\pi_2 = 1/3$ (dotted line), for the case of salt fingers R_ρ(cr) = 0.62, Eq. (22c), while for diffusive-convection R_ρ(cr) = $(0.62)^{-1}$

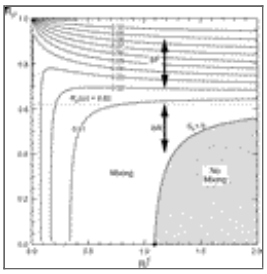

Click on thumbnail for full-sized image.

FIG. 2. Contour plots of the stability function S_h, Eq. (13b), in the Ri^T–R_ρ plane. The zero contour $S_h = 0$ yields Ri^T(cr) above which mixing is no longer present [the values correspond to Eq. (23a) and appendix C]. The value of R_ρ(cr) is also shown

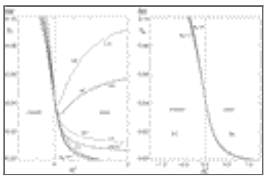

Click on thumbnail for full-sized image.

FIG. 3. (a) The dimensionless stability function S_h for heat diffusivity, Eq. (13b), vs stable Ri^T for different values of R_ρ. Local model, Eq. (16c). Salt fingers (solid line). Diffusive convection (dashed line). We recall that $\mathrm{Ri}^T > 0$ corresponds to dynamical stability while $\mathrm{Ri}^T < 0$ corresponds to dynamical instability. (b) As in (a) but for the DU and DS cases [see definitions after Eq. (4b)]. The values $R_\rho = 0, -0.2, -1, -5$ yield nearly identical results

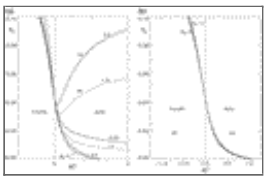

Click on thumbnail for full-sized image.

FIG. 4. (a) Same as in Fig. 3a but for the salinity stability function S_s, Eq. (13c). Note that the curves for the SF and DC cases have exchanged places as compared with Fig. 3a. (b) As in (a) but for the DU and DS cases [see definitions after Eq. (4b)]

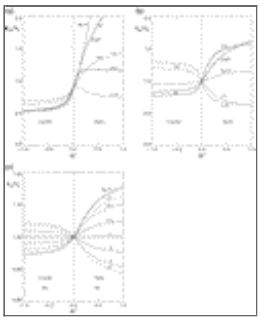

Click on thumbnail for full-sized image.

FIG. 5. (a: top left) The ratio K_m/K_h vs Ri^T; $R_\rho = 0$ corresponds to the laboratory data discussed in Part I. Salt fingers (solid line); diffusive convection (dashed line). (b: top right) The ratio K_s/K_h vs Ri^T for different R_ρ. Salt fingers (solid line). Diffusive convection (dashed line). (c: bottom left) The ratio K_s/K_h vs Ri^T for different R_ρ. Cases DU and DS [see definitions after Eq. (4b)]

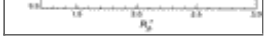

Click on thumbnail for full-sized image.

FIG. 6. The heat-to-salt flux ratio $(K_h/K_s)R^{-1}{}_\rho$ vs $R^{-1}{}_\rho$. In the SF region, we have taken Ri^T very large while in the WR (wave-dominated region), Ri^T is computed using (23c). This result compares well with Fig. 2 of Walsh and Ruddick (2000)

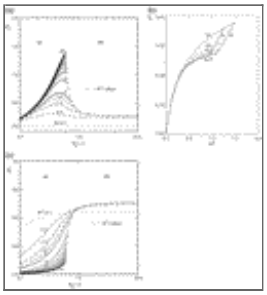

Click on thumbnail for full-sized image.

FIG. 7. (a: top left) The heat mixing efficiency $\Gamma_h = K_h N^2 \epsilon^{-1}$ vs $R^{-1}{}_\rho - 1$ for different stable Ri^T. Using NATRE data, St. Laurent and Schmitt (1999, Fig. 8) have suggested a way to interpret the dependence of Γ_h on Ri^T. Although it is not easy to make a one-to-one correspondence with their work, the general trend predicted by the model in the SF region agrees with the data: the smaller the shear, the larger the Γ_h. (b: top right) The heat mixing efficiency $\Gamma_h = K_h N^2 \epsilon^{-1}$ vs stable Ri^T for different R_ρ. The two lines A and B correspond to $c = 0.85$ and $c = 1$, where c is the parameter entering Eq. (23c). Since the curves bend over, their sensitivity to c decreases. For a given R_ρ, the effect of changing c on Γ_h is not large. In this paper, $c = 0.85$. (c: bottom left) The mass mixing efficiency $\Gamma_\rho = K_\rho N^2 \epsilon^{-1}$ vs $R^{-1}{}_\rho - 1$ for different stable Ri^T. In the WR regime a value $\Gamma_\rho = 0.2$ is usually employed in the literature (Osborn and Cox 1972; Schmitt 1994; St. Laurent and Schmitt 1999). Here, it is derived within the model.

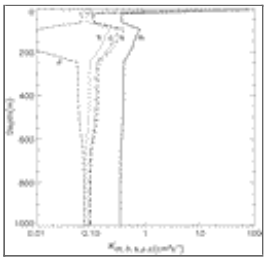

Click on thumbnail for full-sized image.

FIG. 8. The five diffusivities for momentum (m), heat (h), salt (s), mass (ρ), and passive scalar (c) vs depth for the location corresponding to the NATRE measurements

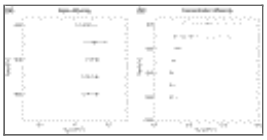

Click on thumbnail for full-sized image.

FIG. 9. (a) Testing the diffusivity model without an OGCM. Mass diffusivity K_ρ compared with NATRE data (diamonds with error bars; St. Laurent and Schmitt 1999). Model results are represented by squares with error bars. (b) Same as (a) but for the concentration diffusivity K_c [triangles from NATRE data from Ledwell et al. (1993, 1998)]

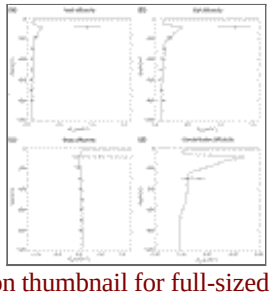

Click on thumbnail for full-sized image.

FIG. 10. Testing the diffusivity model with an OGCM. (a) Heat diffusivity K_h compared with NATRE data [diamonds with error bars from St. Laurent and Schmitt (1999)]. Model results are represented by a solid line. (b) As in (a) but for salt diffusivity K_s. (c) As in (a) but for mass diffusivity K_ρ. (d) As in (a) but for the concentration diffusivity K_c [triangles from NATRE data from Ledwell et al. (1993, 1998)]

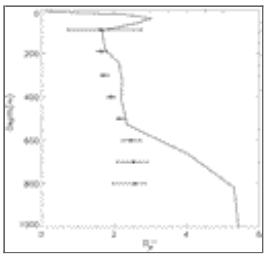

Click on thumbnail for full-sized image.

FIG. 11. Profile of the density ratio R_ρ. NATRE data (diamonds with error bars) and model results (full line)

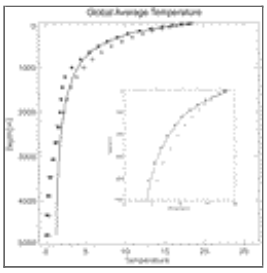

Click on thumbnail for full-sized image.

FIG. 12. The global ocean temperature using the NCAR OGCM. The Levitus et al. (1994) data are represented by a solid line. We have also run the code with the KPP model ($K_s = K_h$, Large et al. 1994) the results of which are represented by diamonds while the present model results are indicated by asterisks

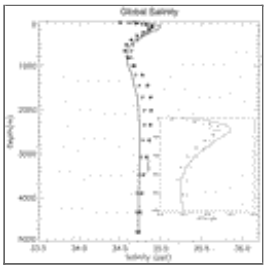

Click on thumbnail for full-sized image.

FIG. 13. As in Fig. 12 but for the global salinity profile

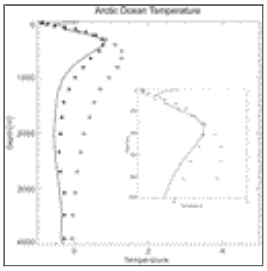

Click on thumbnail for full-sized image.

FIG. 14. As in Fig. 12 but for the Arctic Ocean temperature profile

Click on thumbnail for full-sized image.

FIG. 15. As in Fig. 12 but for the Arctic Ocean salinity profile

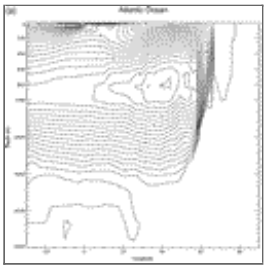

Click on thumbnail for full-sized image.

FIG. 16. The North Atlantic overturning streamfunction (in Sv) with double diffusion (a) and with the present model (b) but with $K_s = K_h$

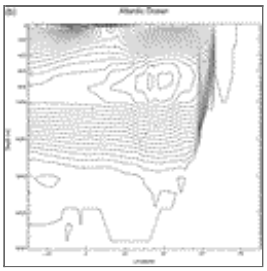

Click on thumbnail for full-sized image.

FIG. 16. (*Continued*)

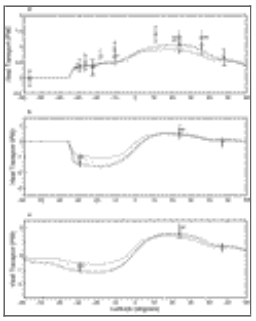

Click on thumbnail for full-sized image.

FIG. 17. Polar heat transport vs latitude for (a) the North Atlantic Ocean, (b) the Indo–Pacific Ocean, and (c) the global ocean. The data from different authors and the error bars are from Macdonald and Wunsch (1996). Solid line (KPP model, $K_s = K_h$), dotted line (present model with $K_s = K_h$), dashed line (present model with $K_s \neq K_h$). Double diffusion ($K_h \neq K_s$) lowers the value of the heat flux, a conclusion in agreement with previous authors

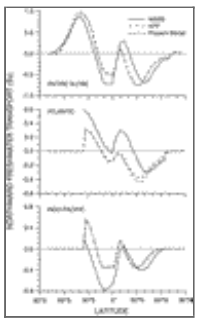

Click on thumbnail for full-sized image.

FIG. 18. Freshwater budget. The WSBS curve corresponds to the measurements of Wijffels et al. (1992) as presented in Large et al. (1997)

Corresponding author address: Dr. V. M. Canuto, NASA Goddard Institute for Space Studies, 2880 Broadway, New York, NY 10025. E-mail: acvmc@giss.nasa.gov

top